Location of Zn within the $Mg_{12}(La_xCe_{1-x})$ lattice by X-ray incoherent channelling patterns

C. J. Rossouw,* C. J. Bettles, T. J. Davis, C. T. Forwood, P. R. Miller and K. Venkatesan

CSIRO Manufacturing Science and Technology, Private Bag 33, Clayton South MDC, Victoria 3169, Australia. Correspondence e-mail: chris.rossouw@cmst.csiro.au

Systematic electron diffraction studies on intermetallic precipitates formed within a lightweight Mg–RE–Zn alloy (RE = La or Ce) identify these to be of structural type $Mn_{12}Th$ (space group $I4/mmm$). Analytical electron microscopy yields an overall composition of $Mg_{12}(La_xCe_{1-x})$ with $x \sim 0.43$, with 1 at.% Zn incorporated within the lattice. Variations in characteristic X-ray emission rates, as an electron beam is rocked near zone-axis orientations, are used to form two-dimensional channelling patterns, termed X-ray incoherent channelling patterns. This channelling contrast enables a specific sublattice site that is occupied by Zn to be unambiguously identified within the $Mg_{12}RE$ lattice. The particular sublattice site is denoted by the Wyckoff letter f, and is one of the three different Mg sublattice sites f, i and j. Of these three sites, the Wigner–Seitz cell that is centred on the f sublattice site has the largest Mg–RE interatomic distance, and therefore the f site is expected to be favoured for accommodating the substitution of a larger Zn atom.

1. Introduction

Various signals, such as those derived from back-scattered electrons or X-rays, may be monitored as a function of angle of incidence of the fast electron onto the crystal target as the collimated electron beam is systematically rocked in angle. This is schematically illustrated in Fig. 1. Note that, whilst the beam is being rocked, the probe remains (as far as possible) on a fixed area. Two-dimensional channelling contrast in an X-ray incoherent channelling pattern (ICP) is due to variations in emission rates of characteristic X-rays with angle of incidence when the electron beam is aligned near a low-index zone axis.

The technique of atom location by channelling-enhanced microanalysis (ALCHEMI) generally involves a correlation of contrast associated with an introduced minority atomic species with channelling contrast derived from each of the majority (or host) atomic species (Tafto & Spence, 1982; Rossouw *et al.*, 1989; Walls, 1992). Statistical ALCHEMI involves a reconstruction of experimental channelling contrast from minority species with a best-fit linear combination of host-atom ICPs, derived from the same experimental data set. Partitioning of the introduced minority species over substitutional sites, together with uncertainties, are subsequently derived from fitted coefficients and their standard deviations (Rossouw *et al.*, 1996; Anderson, 1997). Calculated channelling patterns (Oxley *et al.*, 1999), although providing insight into expected contrast, are not necessary for simple ALCHEMI.

However, this situation is radically different if the atomic species under investigation is either

(i) not distributed over substitutional sites in a way that can be reconstructed from the host-atom distributions, or

(ii) located on interstitial sites.

Under these conditions, the usual formulations of ALCHEMI, using experimental data alone, are not useful. Calculated channelling patterns are now necessary to identify characteristic features associated with individual sublattice or interstitial sites (Rossouw & Miller, 1999; Krishnan *et al.*, 1985). In this work, we identify, from three crystallographically inequivalent sites for the same 'host' atomic species, one specific sublattice site on which a substituted minority atomic species is located that yields an ICP that cannot be reconstructed from a linear superposition of 'host' atom ICPs.

2. Crystal-type determination

The as-cast microstructure of a magnesium–rare-earth–zinc alloy is shown in a scanning electron micrograph in Fig. 2(a), where it is evident that two distinct phases exist, *i.e.* a magnesium solid solution matrix (marked **A**) and an intermetallic interdendritic phase (marked **B**). The crystal structure and the location of Zn within the lattice of this intermetallic phase is the subject of this paper. The total energy-dispersive X-ray (EDX) spectrum after collection of ICP data is shown in Fig. 2(b). Analysis of EDX spectra from thinner areas yielded the composition (in atomic percent) as approximately 92% Mg, 3.3% La and 4.4% Ce, with a small amount (~1%) of Zn and even smaller amounts (less than

Table 1
Atomic labels and coordinates for $Mg_{12}RE$.

Unit cell is tetragonal with $a = 10.31$ and $c = 6.04$ Å (space group $I4/mmm$). Equivalent positions are found by $(000) + (\frac{1}{2}\frac{1}{2}\frac{1}{2})$, and x and y coordinates may be exchanged.

Atom	Number per cell Wyckoff letter		Coordinates x	y	z
Mg	8	f	$\pm\frac{1}{4}$	$\pm\frac{1}{4}$	$\frac{1}{4}$
Mg	8	i	±0.361	0	0
Mg	8	j	±0.277	$\frac{1}{2}$	0
La, Ce (RE)	2	a	0	0	0

Table 2
Half-width at half-maxima b_y for E_o of 200 keV and mean free paths for X-ray absorption λ_y.

Atom	E_y (keV)	b_y (pm)	λ_y (µm)
Mg	1.32	9.7	1.84
La	5.92	3.2	18.7
Ce	6.14	3.0	20.8
Zn	9.68	2.3	36.8

0.1%) of Cu present in the intermetallic phase. Thus, the overall stoichiometry is close to $Mg_{12}RE$, where RE is La or Ce, with a composition ratio La:Ce of about 43:57.

Fig. 3(a) shows a segment of the pole-figure map for this phase, as derived from electron diffraction patterns. This established that the unit cell is tetragonal with lattice parameters $a = 10.3$ Å and $c/a = 0.586$, showing that it conforms with the general structural type $Mn_{12}Th$ (space group $I4/mmm$, No. 139) (Pearson, 1985; Daams et $al.$, 1991). As shown in the stereopair representation of this unit cell in

Fig. 3(b), the rare earth (RE) is uniquely distributed over one particular sublattice site, denoted by the Wyckoff letter a, and located at the origin and body centre of the tetragonal unit cell. Mg is uniformly distributed over three separate sets of sublattice sites within this cell, denoted by Wyckoff letters f, i and j. General atomic coordinates for these four distinct sublattice sites are shown in Table 1.

3. Theory for X-ray incoherent channelling patterns

A theoretical framework within which ICP contrast can be calculated using a Bloch-wave model has been described by Rossouw et $al.$ (1997). The rate of characteristic X-ray emission, $F_y^s(t)$, is expressed in terms of the relative yield under dynamical diffraction conditions compared with that expected if no diffraction or X-ray absorption were to occur. This depends on atom type y and location τ_y within the lattice, as well as crystal orientation s and thickness t. The model also includes a 'background' term due to X-ray generation by

(a)

(b)

Figure 2
(a) SEM micrograph of the two phases in the Mg–RE–Zn alloy (see text). The magnesium solid-solution matrix is marked **A** and the intermetallic phase is marked **B**. (b) Total EDX spectrum after collection of X-ray ICPs from intermetallic phase.
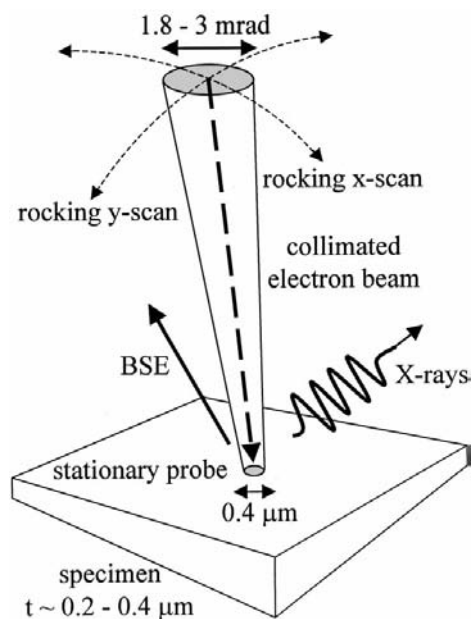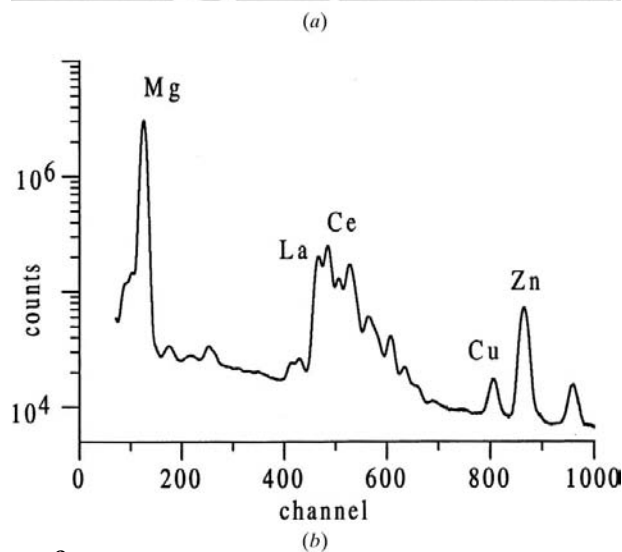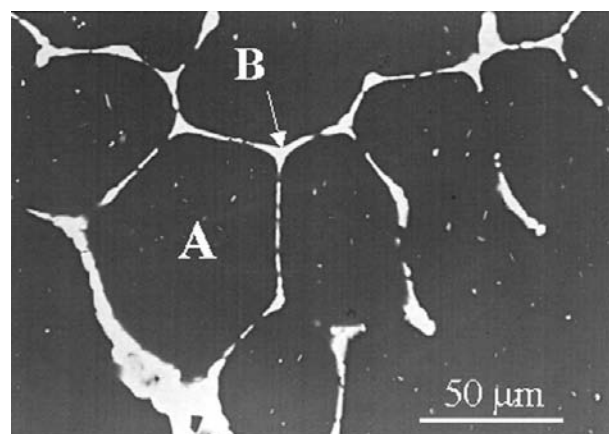

Figure 1
Schematic diagram showing acquisition of channelling patterns from back-scattered electrons or characteristic X-rays as the static electron probe is rocked in angle.

electrons which have been 'dechannelled' due to thermal diffuse scattering (TDS), this contribution being calculated on an Einstein model. An orientation-independent mean absorption, due to delocalized electronic scattering processes, is also included in the model (a mean free path of λ_o being ascribed to this mean absorptive process).

A thermally smeared Lorentzian potential, characterized by a half-width at half-maximum b_y, is used to account for effects of interaction delocalization. Oxley & Allen (2000) have used Hartree–Fock wavefunctions for the bound state of the target electrons, with continuum states being described *via* a Hartree–Slater potential. Their numerical evaluation of inner-shell ionization for K- and L-shell electrons has yielded tables of atomic form factors for ionization. These are dependent on incident-beam energy, threshold ionization energy E_y and type of excitation (K, L, M *etc.*). A reconstruction of the real-space projected potential from this set of data demonstrates that the total ionization process is fairly well described by a Lorentzian potential, where b_y is generally about 60–70% of the impact parameter calculated from the Pennycook (1988) model. Lastly, thickness-integrated absorption of the characteristic X-rays is calculated from the mean free path for X-ray absorption λ_y and specimen–detector geometry. These parameters are given in Table 2 for each atomic species.

The specimen–detector geometry is specified by a factor $R = \cos\theta / \sin(\theta + 20°)$, where the detector take-off angle is 20° and the goniometer tilt towards the detector (mounted at 90° to the goniometer axis) is θ. The mean free path λ_y for absorption of characteristic X-rays from atom y is $1/\mu_y\rho$, where μ_y is the mass absorption coefficient and ρ the density (Heinrich, 1986), and absorption of X-rays within the crystal is accounted for by terms containing Rt/λ_y.

$F_y^s(t)$ is written as a sum of two terms: a 'dynamic' term $D_y^s(t)$, due to ionization from the channelled electron wavefunc-
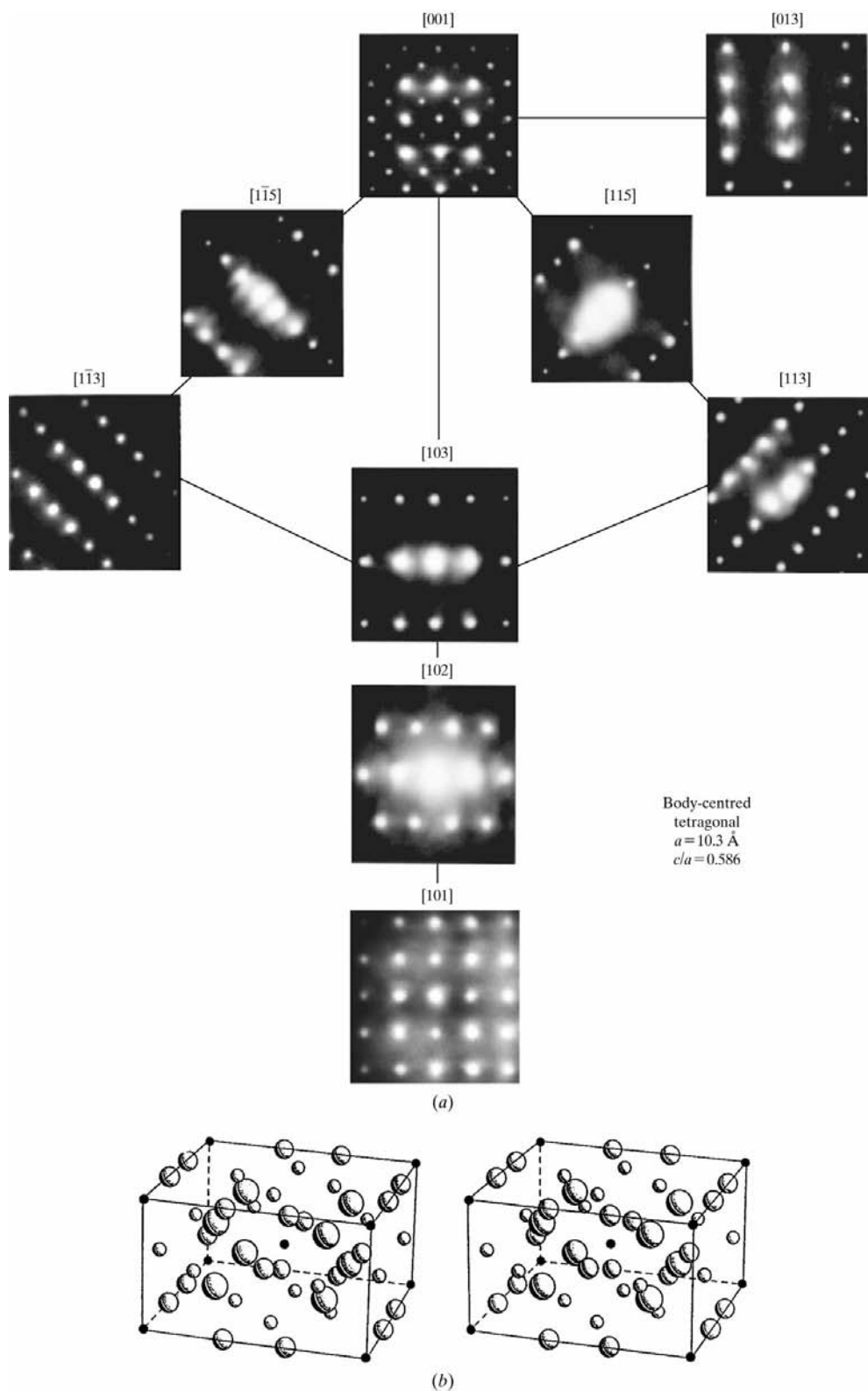

Figure 3
(*a*) Zone-axis pole-figure map from the intermetallic phase to establish unit-cell parameters and general structural type. (*b*) Stereo pair of tetragonal unit cell with sublattice sites *a* are represented by small filled circles, and sites *f*, *i* and *j*, respectively, by the large to small shaded spheres. The *c* axis is vertical.

tion, and a 'kinematic' term $K_y^s(t)$, due to ionization from dechannelled or 'absorbed' electrons. These are given by

$$D_y^s(t) = \sum_{ij} B_y^{ij}(t) \sum_{gh} C_g^i C_h^{j*} M_y(\mathbf{h}, \mathbf{g})/M_y(\mathbf{o}, \mathbf{o}) \qquad (1)$$

and

$$K_y^s(t) = \left[\frac{1 - \exp(-Rt/\lambda_y)}{Rt/\lambda_y}\right] - \sum_i B_y^{ii}(t). \qquad (2)$$

$B_y^{ij}(t)$ is an interference term between Bloch waves of index i and j,

$$B_y^{ij}(t) = \alpha^i \alpha^{j*} \frac{\exp(i\Delta_y^{ij}t) - 1}{i\Delta_y^{ij}t} \qquad (3)$$

and Δ_y^{ij} is defined as $\mathbf{k}^i - \mathbf{k}^{j*} + \mathbf{n}iR/\lambda_y$, where $\mathbf{n}$ is an inward-directed surface normal of unit magnitude and $\mathbf{g}$ and $\mathbf{h}$ are reciprocal-lattice vectors. α^i and C_g^i are complex amplitudes and eigenvector components, respectively, for Bloch state φ^i, and $\mathbf{k}^i$ is the complex eigenvalue $(\gamma^i + i\eta^i)\mathbf{n}$. Equivalently, the mean free path for absorption of the partial wave φ^i can be written $\lambda^{(i)} = 1/2\eta^i$. An overall 'mean' absorption due to delocalized interactions is accounted for by due inclusion of λ_o. The absorptive component is derived from eigenanalysis of
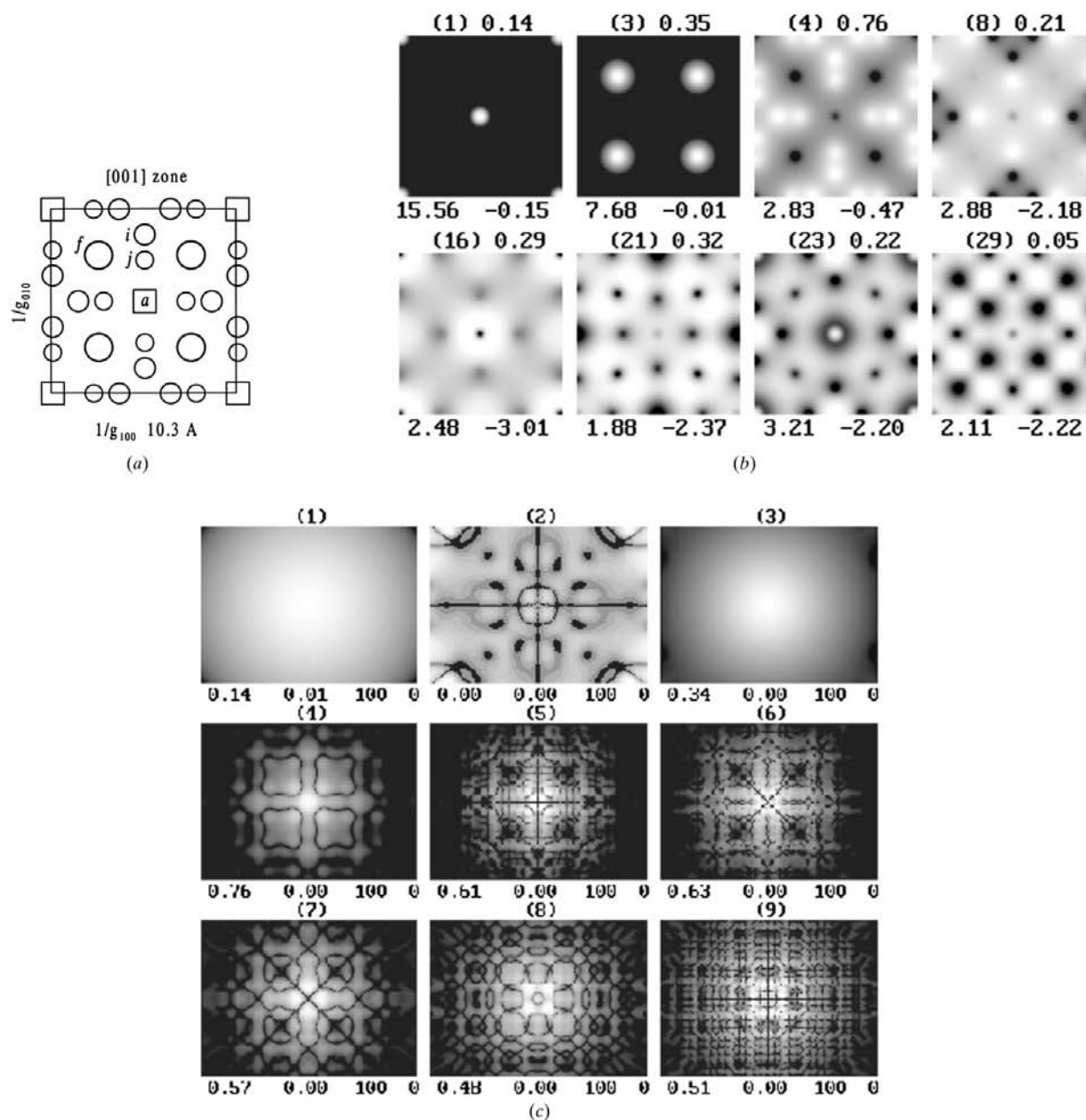

Figure 4
(a) Projected ⟨001⟩ Mg₁₂RE structure, showing the three Mg sites *f*, *i* and *j* (large to small open circles) together with the La and Ce sites *a* = RE (open squares). (b) Bloch waves $\varphi^i(\mathbf{r})$ excited at symmetrical zone-axis orientations shown below, with index (*i*) and excitation amplitude α^i (above) and amplitude range (below). (c) Excitation amplitudes α^i for *i* = 1–9.

the interaction of the fast-electron wavefunction with the elastic and absorptive potentials. Non-local interaction terms of type $M_y(\mathbf{h},\mathbf{g})$ in (1) are approximated to 'local' terms $M_y(\mathbf{g} - \mathbf{h})$, using a localized model for inner-shell ionization. This requires appropriate distribution over interaction sites τ_{ny} within the unit cell, i.e.

$$M_y(\mathbf{g} - \mathbf{h}) = A_y(\mathbf{g} - \mathbf{h}) \sum_n \exp\left[i(\mathbf{g} - \mathbf{h})\tau_{ny}\right], \qquad (4)$$

where a Fourier transform of the real-space (Lorentzian) interaction potential, smeared by Debye–Waller factors, is used to evaluate $A_y(g)$. For a Lorentzian potential $A_y(x)$ of half-width at half-maximum b_y,

$$A_y(g) = [\pi \exp(-gb_y)/b_y][\exp(-W_g)], \qquad (5)$$

where the first term is the Fourier transform of the Lorentzian and the second term accounts for thermal smearing by the Debye–Waller factor $W_g = \langle u_y^2 \rangle g^2/2$, where $\langle u_y^2 \rangle$ is the mean square thermal displacement from equilibrium (Allen & Rossouw, 1993; Cherns *et al.*, 1973). Note that in these equations the reciprocal-lattice vectors have been multiplied by a factor of 2π.

4. Experimental

X-ray ICPs were recorded using a collimated and focused 200 keV electron probe, 0.4 μm in diameter and with total convergence angle of either 1.8 mrad (30 μm condenser aperture) or 3 mrad (50 μm aperture). The intermetallic phase was tilted such that the beam was aligned close to various low-
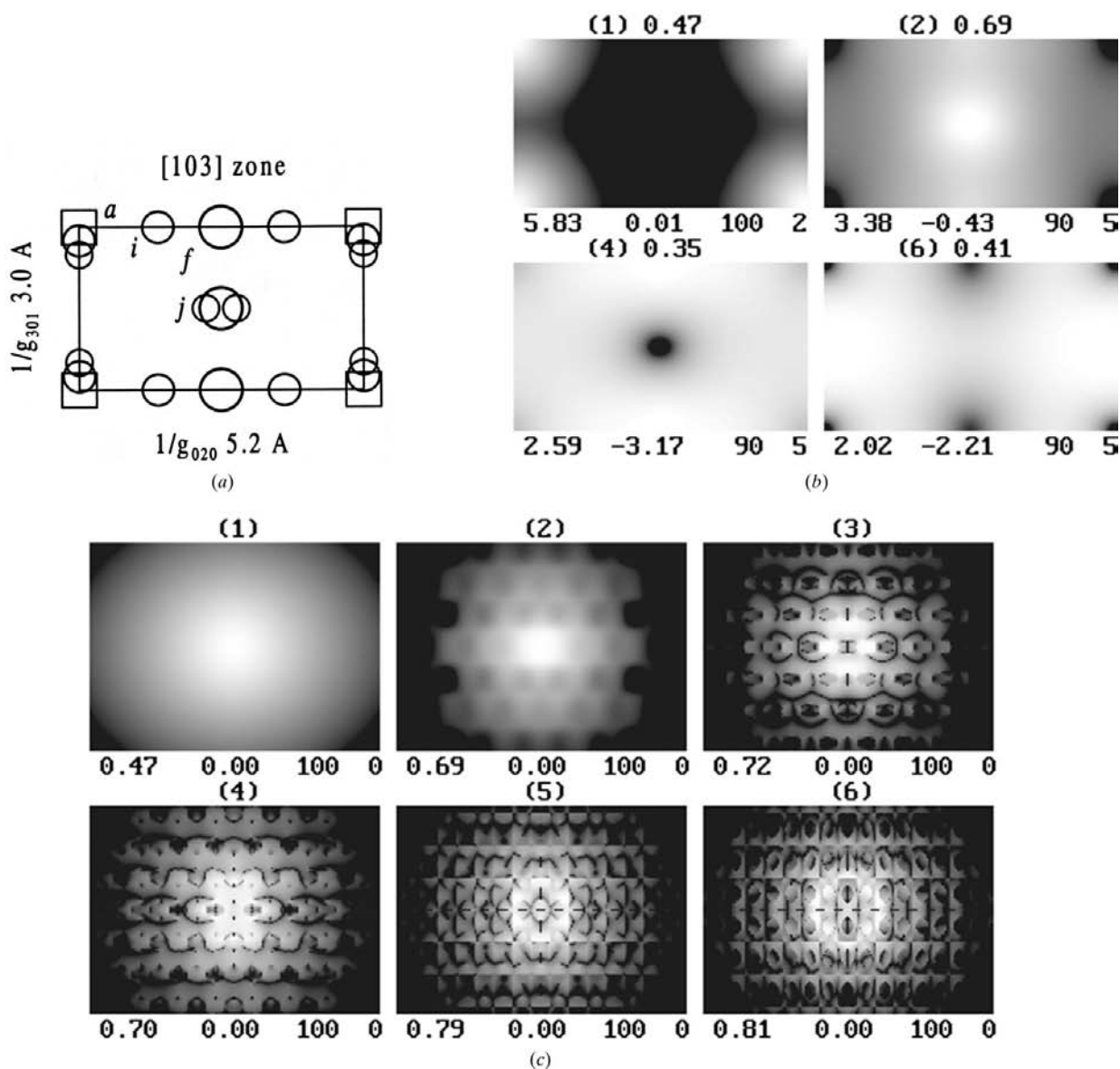

Figure 5
(a) Projected ⟨103⟩ structure, showing three sublattice sites *f, i* and *j* (large to small circles) and sites *a* (squares). (b) Zone-axis states $\varphi^i(\mathbf{r})$ with (i) and α^i given above, amplitude range below. (c) Excitation amplitudes α^i for $i = 1$–6.

Table 3
Binding energies $E^{(i)}$ and TDS $\lambda^{(i)}$ for zone-axis Bloch states i.

Zone	i	$E^{(i)}$ (eV)	$\lambda^{(i)}$ TDS (µm)
$\langle 001 \rangle$	1	72.8	0.0074
	3	21.4	0.060
	4	8.5	0.224
	8	4.8	0.219
	16	−1.6	0.195
	21	−5.8	0.370
	23	−7.2	0.268
	29	−11.0	0.466
$\langle 103 \rangle$	1	20.7	0.039
	2	8.5	0.236
	4	−1.2	0.194
	6	−3.4	0.255
$\langle 115 \rangle$	1	19.6	0.032
	2	7.4	0.365
	4	2.2	0.255
	6	−3.5	0.166
	9	−9.4	0.357
	12	−12.1	0.575

index zone axes on specimen areas up to 0.4 µm thick. Beam rocking, acquisition and storage of energy-dispersive X-ray (EDX) spectra are computer controlled, with recording time being typically 1–4 s pixel^{-1}. The full EDX spectrum is recorded for each pixel and at relatively high count rates (about $1–3 \times 10^4$ counts s^{-1}), so that variations in characteristic X-ray emission as a function of beam orientation can be subsequently obtained by appropriate curve fitting for each spectrum and for all pixels s. This is displayed as a 79×58 pixel map, corresponding to an angular range of 95 mrad along the x axis. The specimen was tilted in the goniometer by θ up to 30° towards the X-ray detector, with orthogonal holder tilts up to 20° to locate appropriate zone axes. Channelling maps derived from back-scattered electron contrast were primarily used for setting up experimental conditions prior to allocating control to the computer, since this is closely related to contrast formed from X-ray emission (Rossouw *et al.*, 1994). The integrated counts for K-shell excitations of Mg and Zn, and L-shell excitations for La and Ce, were monitored for analysis. For each pattern of the type shown in Figs. 7–11, two numbers at the bottom left give the maximum and minimum count or calculated enhancement factors, and two numbers at the bottom right represent the percentage of the white and black contrast level settings, where these are displayed on a logarithmic scale above the minimum count.

5. Results

5.1. Computations

Projected $\langle 100 \rangle$, $\langle 103 \rangle$ and $\langle 115 \rangle$ crystal structures are shown in Figs. 4(a)–6(a), respectively. The open squares represent the sublattice site a occupied by RE and the large to small open circles represent the three sublattice sites denoted by the Wyckoff letters f, i and j, respectively. For the structural type identified for this intermetallic phase, the Mg atom is uniformly distributed over these three sublattice sites f, i and j,

whilst La or Ce is exclusively accommodated on the sublattice site a.

Each geometrical projection (a) may be correlated with the calculated real-space amplitude $\varphi^i(\mathbf{r})$ in (b) for the most significantly excited states (i) at the symmetrical zone-axis orientation. Indices (i) are ordered from most tightly to least tightly bound states and excitation amplitudes α^i are shown above each map, with the maxima and minima in $\varphi^i(\mathbf{r})$ below each distribution. Antisymmetric imaginary states are not shown since these remain unexcited for the exact zone axis or symmetrical orientation. For the $\langle 001 \rangle$ zone, consideration of 401 beams was necessary for a resolution of 0.65 Å. To achieve a resolution of 0.5 Å, 247 beams were used for the $\langle 115 \rangle$ zone and 187 beams for the $\langle 103 \rangle$ zone axis. Debye–Waller factors $8\pi^2 \langle u^2 \rangle$ were calculated assuming a Debye temperature of 300 K, yielding room-temperature values of 1.59 and 0.28 Å^2 for Mg and La or Ce, respectively, and 0.59 Å^2 for Zn. The contribution of Zn atoms to the elastic and absorptive potentials was not taken into account. The mean inner potential V_o is calculated to be 11 V and, for the isotropic Debye–Waller factors above, the mean free path for TDS of a plane wave is $\lambda \sim 0.47$ µm. Binding energies $E^{(i)}$ and mean free paths $\lambda^{(i)}$ for TDS absorption of zone-axis quantum states for the three zones are shown in Table 3.

The projected structure and real-space amplitudes $\varphi^i(\mathbf{r})$ of the eight most highly excited Bloch waves for the $\langle 001 \rangle$ axis are shown in Figs. 4(a) and (b), respectively. The tightly bound state (1), peaking on sublattice site a, is heavily absorbed by TDS, whereas state (3), with maxima on sublattice site f, is less strongly absorbed. State (4) is localized on both sublattices i and j, and undergoes less thermal attenuation although still more strongly absorbed than a plane wave. State (8) has a predominantly antibonding nature between sublattice sites i and j, and higher-index states tend to channel between atomic sites. Although the $\langle 001 \rangle$ scattering geometry distinguishes well between sublattice sites, the projected potential of 340 V on sublattice site a results in state (1) being both tightly bound ($E^{(1)} = 73$ eV) and heavily absorbed, with $\lambda^{(1)}$ being 74 Å (dependent on the Debye–Waller factor for RE atoms). This is in contrast to data for the other zones in Table 3, and could well explain relatively poor channelling contrast obtained from the $\langle 001 \rangle$ zone (see Fig. 7). Although the sublattice sites are less well discriminated in the $\langle 103 \rangle$ and $\langle 115 \rangle$ projections, the projected potential on site a is reduced to 119 and 146 V, respectively. For these two zones, the most localized Bloch state (1), although still a $1s$-type state peaked on RE, is less tightly bound and undergoes less thermal attenuation than for the $\langle 001 \rangle$ zone. The excitation amplitude α^i of the first nine Bloch states as a function of orientation are displayed in Fig. 4(c). The amplitude of $1s$-type states (1) and (3) diminishes smoothly away from the exact zone-axis orientation, with the localized state (1) being less strongly attenuated than the more delocalized state (3) as the crystal is tilted away from the symmetrical zone-axis orientation. The other states show complex geometry as various Brillouin-zone (BZ) boundaries are crossed. Those with zero excitation at the exact zone-axis orientation are generally imaginary antisymmetric states.

The projected structure and amplitudes for four highly excited Bloch waves at the $\langle 103 \rangle$ zone-axis orientation are shown in Figs. 5(a) and 5(b). State (1) is peaked on site a with some overlap on sites i and j, with binding energy $E^{(1)}$ of 21 eV and $\lambda^{(1)}$ of 393 Å. Other states are less tightly bound than a plane wave, i.e. $E^{(i)} < V_o$, but, although $\lambda^{(i)}$ values are in excess of 0.19 μm, these are more strongly absorbed than a plane wave ($\lambda \sim 0.47$ μm). State (2) is peaked on one of the sites f with some overlap onto sites j, whereas state (6) has maxima near open channels in the structure. The variation in α^i as a function of orientation for the first six states are shown in Fig. 5(c). States (3) and (5) are imaginary and antisymmetric, not excited on an axis. Here only state (1) shows 1s-type behaviour, where the excitation amplitude decays smoothly as successive BZ boundaries are crossed.

The projected structure for the $\langle 115 \rangle$ zone is shown in Fig. 6(a). Six Bloch waves are strongly excited at the exact zone-axis orientation, as shown in Fig. 6(b). State (1) has a binding energy of 20 eV and is of 1s type, peaked on site a, with an absorptive mean free path of 320 Å. State (2) is an antibonding state between sublattice site a and the three sublattice sites f, i and j, with $\lambda^{(2)}$ being 0.36 μm. State (12) propagates with relatively small absorption due to TDS, the absorptive mean free path of 0.58 μm being larger than that of a plane wave. The variation of α^i with orientation is mapped in Fig. 6(c).

5.2. Comparison of experimental with calculated patterns

Experimental channelling patterns from characteristic X-ray emission of Mg, RE and Zn are shown in Figs. 7–9 for the three zone axes, aligned with the real-space projections in Figs 4–6. EDX spectra were recorded with a livetime of 4 s pixel^{-1} and a 3 mrad convergence angle in order to push the count rates up to obtain statistically significant Zn counts for each pixel within a reasonable time. For the $\langle 001 \rangle$ zone, data were collected from an area of thickness ~0.4 μm and with a goniometer tilt of 21°. Data were collected from thicknesses in the range of 0.2–0.5 μm for the $\langle 103 \rangle$ and $\langle 115 \rangle$ zone axes, with goniometer tilts of 1 and 30°, respectively. An overall 'shading' of these channelling patterns occurs with changes in mean specimen thickness from which data are collected. This is attributable to a combination of a shift of the
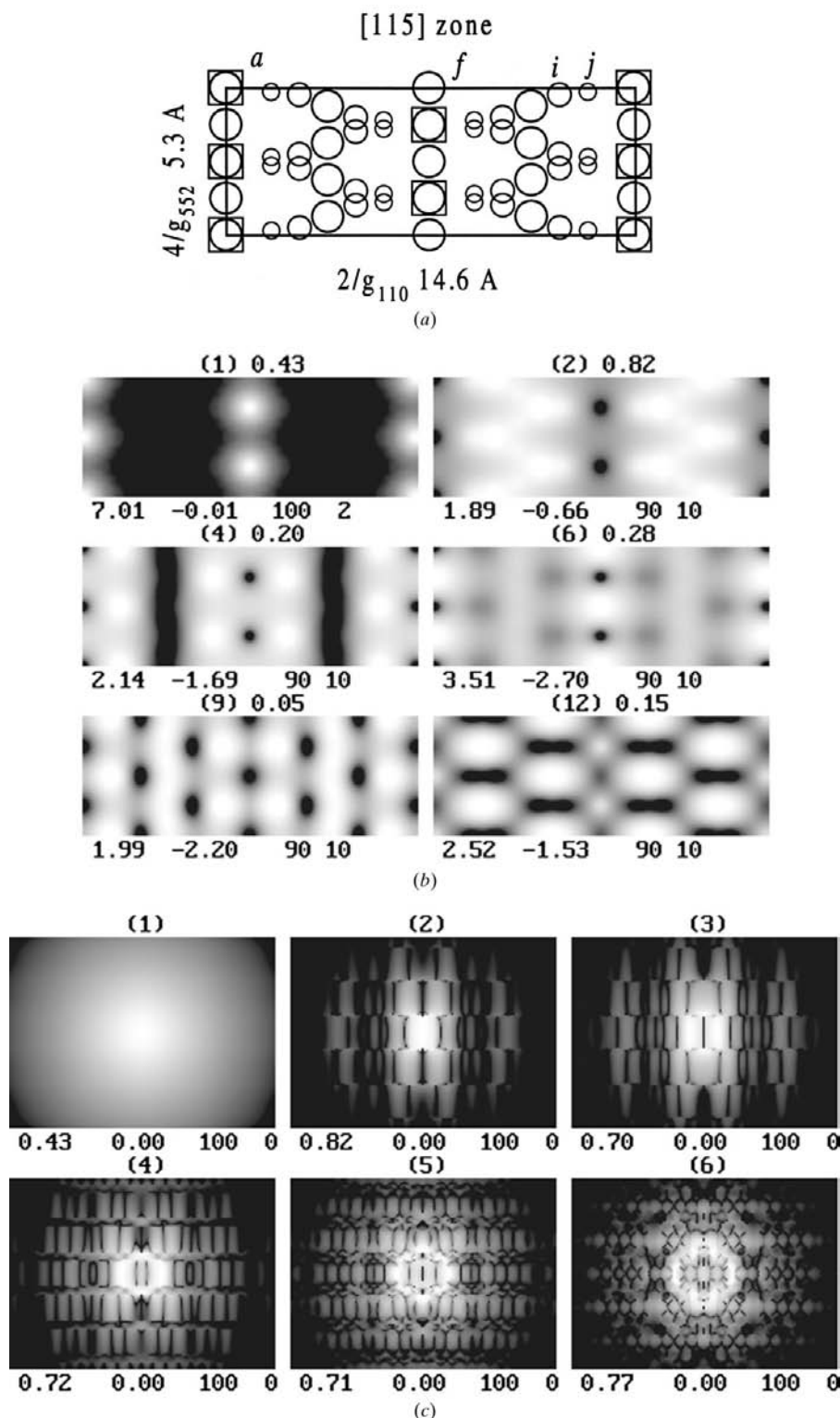

Figure 6
(a) Projected $\langle 115 \rangle$ structure, showing three sublattice sites f, i and j (large to small circles) and sites a (squares). (b) States $\varphi^i(\mathbf{r})$ with (i) and α^i given above, amplitude range below. (c) Excitation amplitudes α^i for $i = 1$–6.
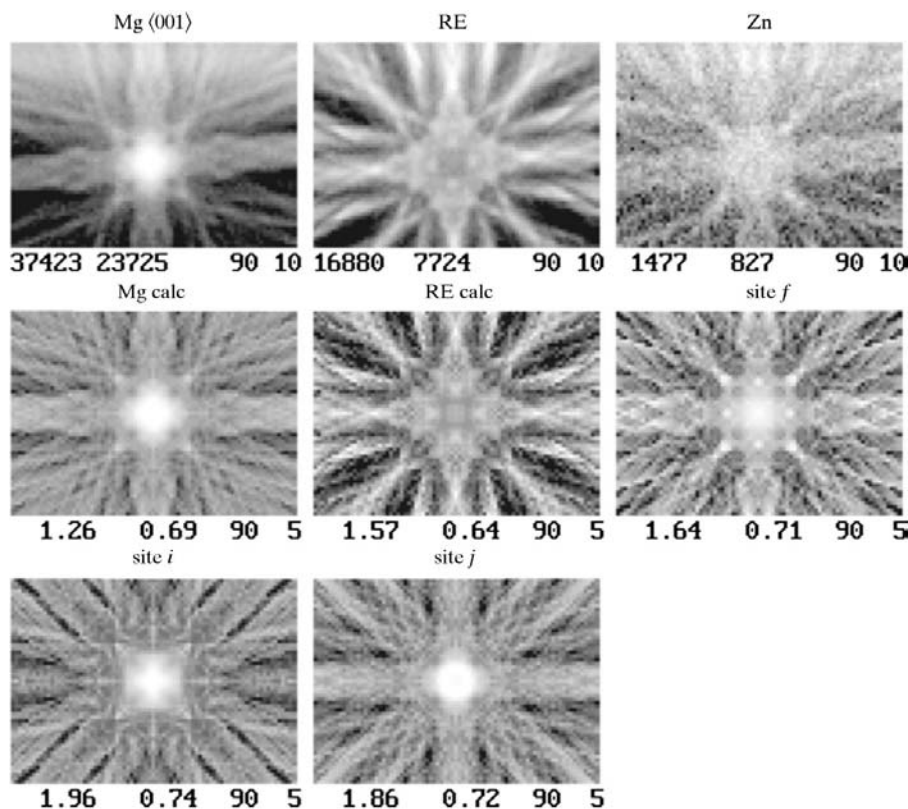
Figure 7
⟨001⟩ zone X-ray ICPs for Mg, RE and Zn aligned with $g_x = 100$ and $g_y = 010$, compared with calculated ICPs for sublattice sites f, i and j.
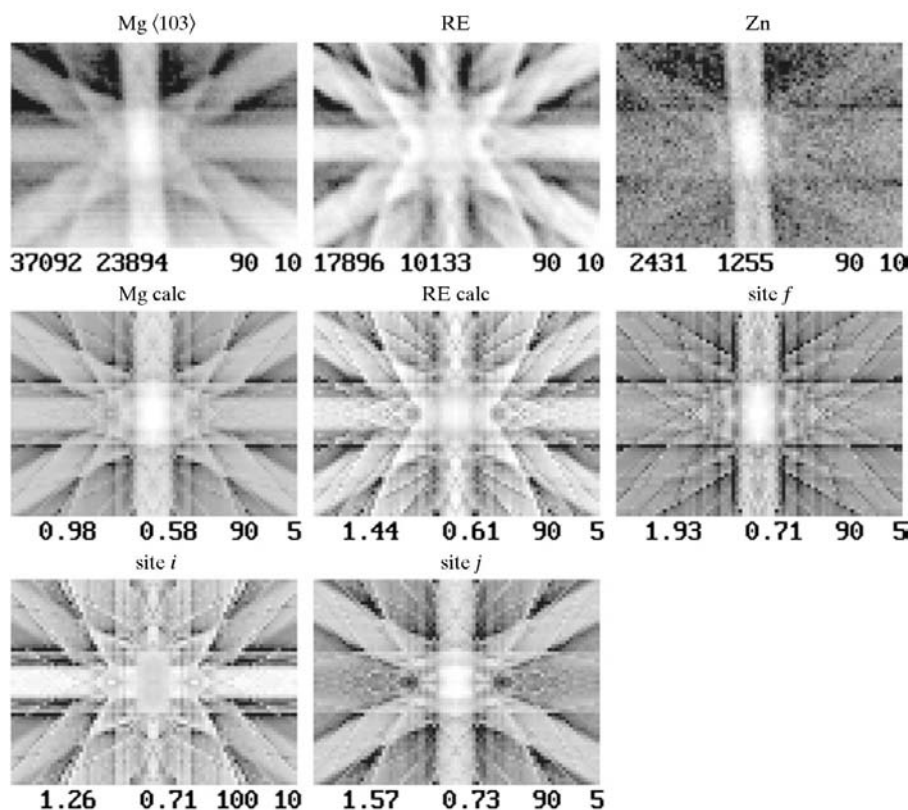

Figure 8
⟨103⟩ zone X-ray ICPs for Mg, RE and Zn aligned with $g_x = 020$ and $g_y = 301$, compared with calculated ICPs for sublattice sites f, i and j.

focused beam during data collection (incurred by effects of lens distortions whilst electronically rocking the beam) and specimen drift and is evident to some extent in each zone-axis pattern. Contrast from La and Ce excitations were indistinguishable and these intensities were summed to form a contribution RE, hence reducing noise in channelling contrast from the sublattice site a.

Channelling contrast for Mg (summed over sublattice sites f, i and j using localization and absorptive parameters in Table 2) and RE (on sublattice site a, and adopting characteristics of Ce in Table 2), as well as the three sites f, i and j, were calculated and are shown in these figures for a thickness of 0.5 μm. Characteristics of Zn from Table 2 were used to compute channelling patterns from each of the sublattice sites f, i and j. An orientation-independent 'mean' absorption, with a mean free path λ_o of 0.5 μm, was also included in the calculations.

Good correlation between experiment and theory for Mg and RE ICPs is evident in Fig. 7 for the ⟨001⟩ zone. However, the Zn response is dissimilar to either Mg or RE, and correlates closely with the calculated response for site f. The other sublattice site 'signatures' differ in detail from the Zn response. The Zn response for the ⟨103⟩ zone in Fig. 8 is once more distinct from either Mg or RE responses, with features such as the vertical pair of excess bands correlating well with the calculated pattern for site f. Once more, responses from sublattice sites i and j differ distinctly from the experimental Zn pattern.

The ⟨115⟩ zone patterns recorded under high-count-rate conditions were affected by shading from top to bottom. For this reason, patterns recorded earlier at lower count rates with a convergence angle of 1.8 mrad and 2 s pixel^{-1} are shown in Fig. 9. Although affected by a larger noise component, it is once more apparent that contrast in the Zn pattern differs from both Mg and RE patterns but that reasonably good correlation again occurs with the features in the calculated pattern for sublattice site f. It should be noted that

correlation between theory and experiment for Mg and RE is good for all three zones, so that the basic assumption of an equal distribution of Mg over sublattice sites *f*, *i* and *j* and exclusive occupation of sublattice site *a* by La or Ce appears valid. Although reasonably noisy, the experimental Zn ICP is not in detail similar to either of the host-atom ICPs, but in each case correlates best with the calculated pattern for site *f*.

In an attempt to sharpen contrast and to nullify effects of varying thicknesses, experimental Zn/RE ratio patterns are shown in Fig. 10 for each zone. These provided a clearer result than Zn/Mg ratio patterns since Mg is distributed partially over the Zn sublattice site *f*. Correlation with three calculated ratio patterns (responses from sites *f*, *i* and *j* normalized by the site *a* response) for each zone enables the sublattice site occupied by Zn to be deduced. For the $\langle 001 \rangle$ zone in Fig. 10(*a*), reasonably good correlation occurs between experimental Zn/RE and the calculated pattern *f*/*a*. Better overall agreement is to be seen for the $\langle 103 \rangle$ zone in Fig. 10(*b*), where correlation is observed between the experimental Zn/RE pattern with the calculated *f*/*a* ratio. The other possible ratio patterns differ considerably from experiment, suggesting that sublattice sites *i* or *j* are not significantly occupied by Zn. By similar argument and observation, the $\langle 115 \rangle$ zone-axis-ratio patterns Zn/Re in Fig. 10(*c*) provide evidence again that Zn is preferentially located on sublattice sites *f* (for this particular data set, ratio patterns were obtained from data recorded at higher count rates than the $\langle 115 \rangle$ patterns shown in Fig. 7).

5.3. Semi-quantitative analysis

In order to derive a numerical solution to the problem of determining the distribution of Zn over sublattice sites $k = f, i$ and j, an approach similar to that for statistical ALCHEMI is used, *i.e.* the experimental pattern is simulated from a linear superposition of scaled calculated patterns, where the scaling factors are related to the occupancy of the particular sublattice site (Rossouw *et al.*, 1996). The whole data set is then used to fit Zn counts N_{Zn}^s for each pixel *s* to a linear summation of calculated counts N_k^s for each sublattice site $k = f, i$ and j via χ^2 minimization techniques, *i.e.*

$$N_{Zn}^s = \sum_{k=1}^3 \beta_k N_k^s + C, \qquad (6)$$

where the factors β_k are fitted constants and *C* an offset constant, and the fractional distribution F_n of Zn over a sublattice site *n* is given by $F_n = \beta_n / \sum_k \beta_k$.

In order to compensate for defects in the model due to imperfect removal of distortions from the experimental pattern, an extra amount of noise was introduced to the experimental counts and count ratios such that χ_R^2 (χ^2 divided by the number of degrees of freedom, about 4500) is returned as unity after the fitting procedures. This required an enhancement of experimental noise by a factor of 2–2.5, thus enabling a realistic estimation of uncertainties in the fitted coefficients β_k. This artificially enhanced noise serves to compensate not only for defects in the model due to imperfect removal of distortions from the experimental patterns but also for other deficiencies built into the model calculations such as neglect of beam convergence angle, non-refinement of thickness and approximations in setting up both the elastic and absorptive potentials.

Geometric distortions and misalignments may be described in terms of translations of the pattern in two dimensions, small rotations, shears and dilatations. On a linear model, these distortions are described via a transformation

$$\begin{pmatrix} x'_n \\ y'_n \end{pmatrix} = \begin{pmatrix} a & b \\ c & d \end{pmatrix} \begin{pmatrix} x_n \\ y_n \end{pmatrix} + \begin{pmatrix} t_x \\ t_y \end{pmatrix}, \quad (7)$$

where (x_n, y_n) are the column and row number of pixel *n* in the distorted experimental image, and (x'_n, y'_n) locate the corresponding point in the undistorted or calculated image. Unknown coefficients *a*, *b*, *c*, *d* determine the image distortions and (t_x, t_y) is a two-dimensional translation vector. These unknown parameters are found using a least-squares minimization procedure based on a large number of pairs of
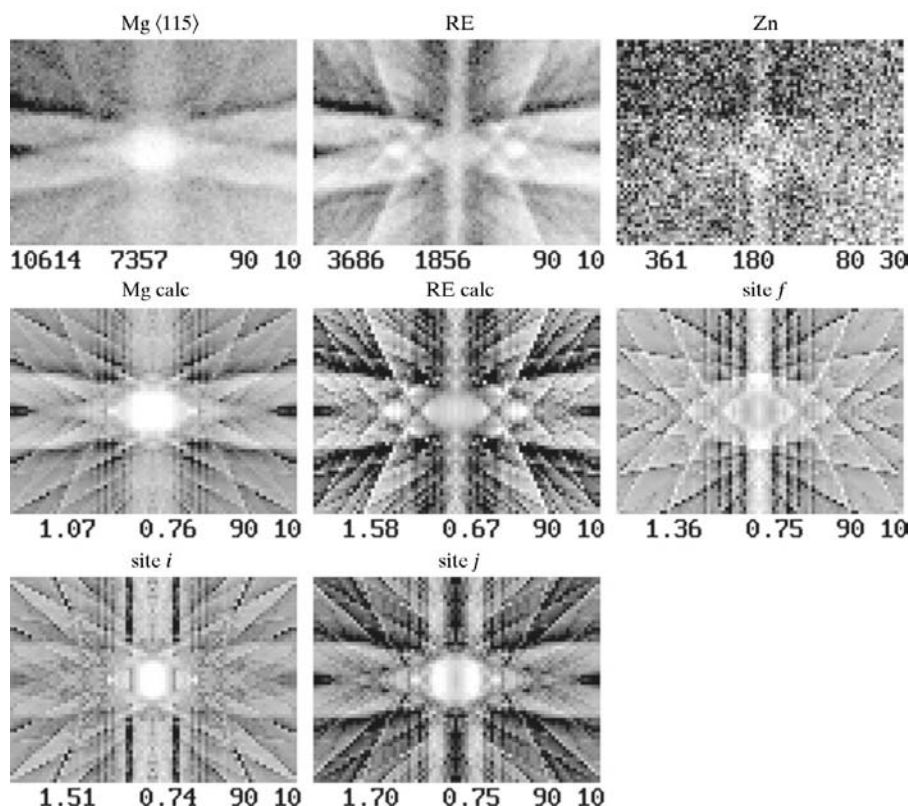

Figure 9
$\langle 115 \rangle$ zone X-ray ICPs for Mg, RE and Zn aligned with $g_x = 110$ and $g_y = 552$, compared with calculated ICPs for sublattice sites *f*, *i* and *j*.

corresponding points (x_n, y_n) and (x'_n, y'_n) found manually by locating corresponding features in the experimental and computed patterns. For example, by minimizing

$$\chi_G^2 = (1/N) \sum_{n=1}^{N} (x'_n - ax_n - by_n - t_x)^2 \qquad (8)$$

with respect to a, b and t_x, three simultaneous equations are obtained involving averages, such as $\langle x \rangle$, $\langle xx' \rangle$ and so on. Here the subscript G in χ_G^2 is to distinguish this geometrical χ^2 value from the previous value. The solution of the three equations gives the three unknown parameters a, b and t_x. The remaining three parameters are found by minimizing the corresponding equation for y'_n. Once the coefficients are found, equation (7) is used to map experimental data onto calculated data. A simple linear interpolation of image values about the integer coordinate is used to take account of the fractional parts of the coordinates.

A comparison of distortion-corrected Zn and Zn/RE patterns with fitted patterns is illustrated in Fig. 11 for the

$\langle 103 \rangle$ zone. Parts of these patterns that are excluded from the fitting process are shown as an average grey tone, for instance near the top left and both the top and bottom rows. The fractional distribution F_h of Zn over sublattice sites f, i and j is shown in Table 4.

Numerical analysis of Zn patterns for all three zones yielded the following result: For the Zn counts alone, the fraction Zn on sites f varies between 0.59 and 0.71, with the residue mainly on site j. However, analysis of Zn/RE ratio patterns yields between 0.57 and 0.85 of Zn on site f. This analysis is dependent on the accuracy to which experimental distortions may be corrected, and this is not an exact process, given that non-linear distortions are not accounted for. Agreement between results from different zones is not good. Although numerical results are somewhat inconsistent, they do imply that well over 60% of Zn is accommodated on sublattice site f. Considering possible errors in model calculations and distortion corrections, we feel that this somewhat rudimentary numerical analysis is however consistent with the
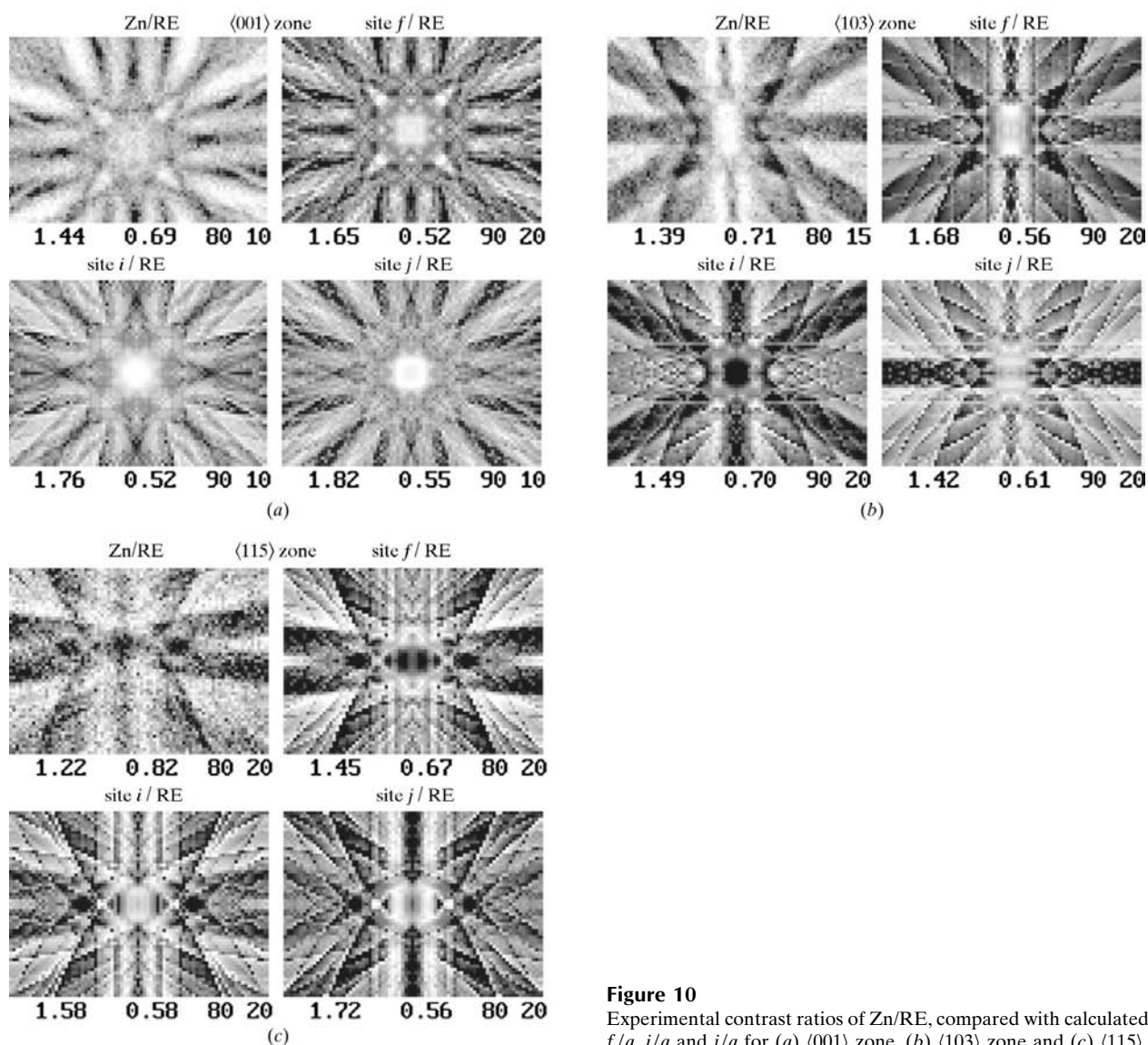

Figure 10
Experimental contrast ratios of Zn/RE, compared with calculated ratios f/a, i/a and j/a for (a) $\langle 001 \rangle$ zone, (b) $\langle 103 \rangle$ zone and (c) $\langle 115 \rangle$ zone.

Table 4
Distribution F_n of Zn over sublattice sites denoted by the Wyckoff letters f, i and j from $\langle 103 \rangle$ zone Zn and ratio Zn/RE analysis.

	n	F_n
Zn analysis	f	0.71
	i	0.01
	j	0.29
Zn/RE analysis	f	0.85
	i	0.06
	j	0.09

Table 5
Nearest-neighbour interatomic spacings (in Å units) between the four sublattice sites denoted by the Wyckoff letters a, f, i and j.

	a	f	i	j
a	6.042	3.946	3.722	3.796
f	–	3.021	3.199	3.000
i	–	–	2.866	3.195
j	–	–	–	3.252

view that Zn is principally if not exclusively accommodated in sublattice site f, as derived in §5.3 from intuitive pattern recognition. However, the inaccuracies of numerical analysis when comparing experiment with calculated patterns does not reflect on the accuracy of statistical ALCHEMI, where numerical analysis of purely experimental results has been shown to be accurate (Rossouw *et al.*, 1996; Anderson, 1997).

6. Discussion

Analysis of X-ray channelling patterns, formed by variations in characteristic X-ray emission rates as a function of electron-beam orientation under zone-axis diffraction conditions, has been taken beyond the usual methods of ALCHEMI. We have been able to identify, from three possible non-equivalent Mg sublattice sites, one particular sublattice site that is favoured by 1 at.% Zn within the $Mg_{12}(La_xCe_{1-x})$ lattice, *i.e.* the Mg sublattice site f is found to be occupied by Zn. A similar problem involving the need to use calculated channelling

patterns to determine the nature of the atomic site occupied by a solute atom was a case where Cr (at a concentration of 6 at.%) within a mullite lattice was found to occupy a unique interstitial site (Rossouw & Miller, 1999).

Referring to Table 5, we find that a major distinction between sublattice sites f, i and j is the interatomic distance to sublattice site a, occupied by La or Ce, where the nearest-neighbour distance is maximized for f (3.95 Å) compared with i (3.72 Å) or j (3.8 Å). Thus, considerations based on the Zn–RE interatomic spacings may explain the fact that Zn favours occupation of sublattice site f.

It has been implicitly suggested by Anderson (1997) that, in order to improve the 'accuracy' of ALCHEMI, channelling maps obtained from predominantly systematic row diffraction conditions ought to be used. There are a few reasons for this. The influence of the localized absorptive potential due to TDS will be less severe, and it is well known that differences in X-ray emissions due to delocalization of the ionization potential are reduced for (essentially) a one-dimensional compression of the probability density of the electron wave-function within the unit cell compared with a two-dimensional compression obtained under zone-axis diffraction conditions. However, two-dimensional X-ray ICPs, for zone axes of the type used here, have distinct advantages over those obtained under systematic row conditions. For a similar specimen thickness, zone-axis diffraction conditions induce a stronger dynamically induced variation in X-ray fluorescence. Resultant channelling patterns have exquisitely fine contrast detail, which is indispensable in enabling intuitive or numerical sublattice site determination of atomic species at low concentrations. Finally, it is easier to match two-dimensional patterns by eye compared with one-dimensional scans, and a greater overall sensitivity to the precise location of the atom within the lattice is obtained.
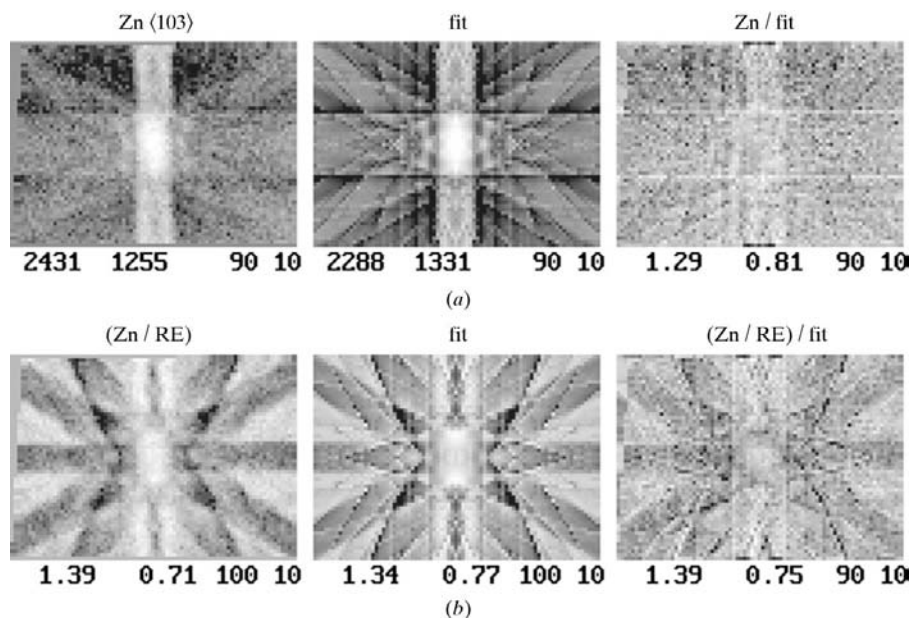
Figure 11
(*a*) Distortion-corrected Zn counts for the $\langle 103 \rangle$ zone, compared with the fitted values from the patterns associated with sublattice sites f, i and j. The ratio Zn/fitted counts is shown. (*b*) Similar to above, but using a fit of Zn/RE to calculated ratio patterns f/a, i/a and j/a. The ratio of experiment to fit is also shown.

References

Allen, L. J. & Rossouw, C. J. (1993). *Phys. Rev. B*, **47**, 2446–2452.

Anderson, I. M. (1997). *Acta Mater.* **45**, 3897–3909.

Cherns, D., Howie, A. & Jacobs, M. H. (1973). *Z. Naturforsch. Teil A*, **28**, 565–571.

Daams, J. L. C., Villars, P. & van Vucht, J. H. N. (1991) *Atlas of Crystal Structure Types for Intermetallic Phases*, p. 4264. Materials Park, OH: ASM International.

Heinrich, K. F. J. (1986). *11th International Congress on X-ray Optics and Microanalysis*, edited by J. D. Brown & R. H. Packwood, pp. 67–72. London, Ontario: The Congress.

Krishnan, K. M., Rez, P. & Thomas, G. (1985). *Acta Cryst.* B**41**, 396.

Oxley, M. P. & Allen, L. J. (2000). *Acta Cryst.* A**56**, 470–490.

Oxley, M. P., Allen, L. J. & Rossouw, C. J. (1999). *Ultramicroscopy*, **80**, 109–124.

Pearson, W. B. (1985). *Pearson's Handbook of Crystallographic Data for Intermetallic Phases*, Vol. 3, edited by P. Villars & L. D. Calvert, p. 2696. Metals Park, OH: American Society for Metals.

Pennycook, S. J. (1988). *Ultramicroscopy*, **26**, 239–248.

Rossouw, C. J., Forwood, C. T., Gibson, M. A. & Miller, P. R. (1996). *Philos. Mag.* A**74**, 57–76, 77–102.

Rossouw, C. J., Forwood, C. T., Gibson, M. A. & Miller, P. R. (1997). *Micron*, **28**, 125–137.

Rossouw, C. J. & Miller, P. R. (1999). *Am. Mineral.* **84**, 965–969.

Rossouw, C. J., Miller, P. R., Josefsson, T. W. & Allen, L. J. (1994). *Philos. Mag.* A**70**, 985–998.

Rossouw, C. J., Turner, P. S., White, T. J. & O'Connor, A. J. (1989). *Philos. Mag. Lett.* **60**, 225–232.

Tafto, J. & Spence, J. C. H. (1982). *Ultramicroscopy*, **9**, 243–249.

Walls, M. G. (1992). *Microsc. Microanal. Microstruc.* **3**, 443–451.